· Article · Advances in Polar Science
doi: 10.13679/j.advps.2021.0012 June 2021 Vol. 32 No. 2: 141-160

A case study based on ground observations of the conjugate ionospheric response to interplanetary shock in polar regions

HE Fang*, HU Zejun, HU Hongqiao, HUANG Dehong & YU Yao

MNR Key Laboratory for Polar Science, Polar Research Institute of China, Shanghai 200136, China

Received 13 April 2021; accepted 4 June 2021; published online 20 June 2021

Abstract Data acquired by imaging relative ionospheric opacity meters (riometers), ionospheric total electron content (TEC) monitors, and three-wavelength auroral imagers at the conjugate Zhongshan station (ZHS) in Antarctica and Yellow River station (YRS) in the Arctic were analyzed to investigate the response of the polar ionosphere to an interplanetary shock event induced by solar flare activity on July 12, 2012. After the arrival of the interplanetary shock wave at the magnetosphere at approximately 18:10 UT, significantly enhanced auroral activity was observed by the auroral imagers at the ZHS. Additionally, the polar conjugate observation stations in both hemispheres recorded notable evolution in the two-dimensional movement of cosmic noise absorption. Comparison of the ionospheric TEC data acquired by the conjugate pair showed that the TEC at both sites increased considerably after the interplanetary shock wave arrived, although the two stations featured different sunlight conditions (polar night in July in the Antarctic region and polar day in the Arctic region). However, the high-frequency (HF) coherent radar data demonstrated that different sources might be responsible for the electron density enhancement in the ionosphere. During the Arctic polar day period in July, the increased electron density over YRS might have been caused by anti-sunward convection of the plasma irregularity, whereas in Antarctica during the polar night, the increased electron density over ZHS might have been caused by energetic particle precipitation from the magnetotail. These different physical processes might be responsible for the different responses of the ionosphere at the two conjugate stations in response to the same interplanetary shock event.

Keywords **polar ionosphere, conjugate, interplanetary shock, response, irregularity**

Citation: He F, Hu Z J, Hu H Q, et al. A case study based on ground observations of the conjugate ionospheric response to interplanetary shock in polar regions. Adv Polar Sci, 2021, 32(2): 141-160, doi: 10.13679/j.advps.2021.0012

1 Introduction

The interaction between the solar wind and the magnetosphere-ionosphere coupling system in polar regions has long been a popular topic in space physics. The energy of the solar wind penetrates into near-Earth space via magnetic reconnection and is released into the ionosphere. Because of the specific configuration of the geomagnetic field in polar regions, the ionosphere over the geomagnetic-conjugate Arctic and Antarctic regions presents similar or identical local response characteristics with respect to magnetospheric energy release. The conjugate study of both hemispheres is of great significance for identifying the physical processes of energy transfer in the magnetosphere-ionosphere coupling system.

Conjugate observation of auroral phenomena was initiated by DeWitt (1962) using the Campbell Island-Farewell Alaska station pair. The occurrence of similar forms and motions and the simultaneous breakup of auroras

* Corresponding author, ORCID: 0000-0001-6781-6977, E-mail: hefang@pric.org.cn

at the conjugate points were confirmed. Wescott's (1966) analysis of all-sky camera data acquired by the Syowa Station and Reykjavik conjugate pair followed. It was found that the conjugacy at these latitudes was not as good as that of the pair studied by DeWitt. Then, a conjugate aircraft observation experiment was carried out from 1967 to 1971 by the University of Alaska. Several papers based on this experiment were published (Belon et al, 1969; Stenbaek-Nielsen et al., 1972, 1973, 1997). The analyses showed that the conjugacy of auroras was well maintained at invariant latitudes of 63–65° but was less well maintained at invariant latitudes greater than 65°. The differences in conjugate auroral intensity at different latitudes were also discussed. Sato et al. (1998) investigated the auroral conjugacy and nonconjugacy characteristics using all-sky auroral imager data from the Syowa Station in Antarctica and the Husafell Station in Iceland and suggested that the time lag of the auroral breakup at conjugate points occurred because the trigger source was not located near the magnetospheric equator plane. The conjugate study of the two hemispheres by Ostgaard et al. (2004) suggested that the locations of the substorm onset and auroral features were usually asymmetric because of magnetic tensions acting on the open magnetic field line prior to the magnetic reconnection or the effects of the interplanetary magnetic field (IMF) on the magnetosphere. Martinis et al. (2014) combined geomagnetic conjugate 630.0 nm airglow image data obtained by low- to subauroral-latitude all-sky imager chains and satellite data to study the ionospheric coupling process in both hemispheres and the transfer behavior between the thermosphere and ionosphere.

There were several papers on auroral dynamics following interplanetary shocks. In the two cases reported by Craven et al. (1985), beginning ~30 min after each sudden commencement, the aurora became active and displayed significant variations in its luminosity and spatial distribution. Egeland et al. (1994) analyzed meridian scanning photometer measurements from Longyearbyen in conjunction with particle and field data retrieved by the Dynamics Explorer Satellite and found that softer particle precipitation appeared to have a source near the flanks of the magnetotail, while harder, more equatorward precipitation originated closer to the Earth. Ho and Tsurutani (1997) examined International Sun-Earth Explorer-3 (ISEE-3) distant tail data during three magnetic storms. Nine tail plasma sheet jettings and 12 slow-mode shocks were detected during the three storms, and they suggested that the dynamics of the distant tail were not at all related to magnetic storms and substorms but were an aftereffect. Zhou and Bruce (1999) also presented two cases of abrupt dayside auroral brightening and very fast auroral propagation using ultraviolet imaging data from the Polar satellite. They found that aurora brightening and motion were associated with the arrival and propagation of interplanetary shocks.

However, some studies have focused on comparative analyses of polar ionospheric conjugacy. Greenwald et al. (1990) carried out a comparative study of high-latitude plasma convection patterns under various B_y conditions using two conjugate high-frequency (HF) radars in the polar regions in both hemispheres. Shand et al. (1998) analyzed the difference in the response of the conjugate polar ionosphere to IMF variation using the Polar Anglo-American Conjugate Experiment (PACE) radar system, and they argued that the main contributor to the discrepancies in observations between the polar geomagnetic conjugate regions was the position of the ionospheric convection reversal boundary within the view of the PACE radars. Yeoman et al. (1999) studied the conjugate characteristics of the ionosphere during the growth phase of substorm activity using the HF radars at the Halley Station in Antarctica and Goose Bay Station in the Arctic, with fields of view arranged to provide a sizeable conjugate overlap. The HF radar data presented high conjugate consistency, and a comparison with particle flux data from the Defense Meteorological Satellite Program (DMSP) satellite showed that the area of the radar backscatter was closely related to the particle precipitation on the nightside. Nevertheless, considerable nonconjugacies were present during the expansion phase, which might be attributed to the different local particle acceleration mechanisms.

The aforementioned research indicates that conjugate study in polar regions is of great significance for identifying the physical processes of magnetosphere-ionosphere coupling and its energy transfer process. However, such studies mostly focused on the spatiotemporal evolution characteristics of the polar conjugate ionosphere in a specific layer and lacked simultaneous ground observations of the variation characteristics of the lower ionosphere due to limited observation approaches. Opportunities for conjugate auroral observations using optical methods are very limited because one hemisphere is usually sunlit. Even at equinoxes when dark sky is present at both stations, weather conditions impose other limitations, and the sky must be clear at both points. If one wants to study the conjugacy in summer or winter, it is necessary to introduce other observational means that can operate throughout the year.

In high-latitude regions, the riometer is a popular ionospheric observation instrument, and it is often used as joint observation with HF radar or incoherent scatter radar to identify the spatiotemporal evolution features of the ionospheric irregularity and electron density at different altitudes. Hargreaves et al. (2007) used incoherent scatter radar, an imaging riometer and satellite data to analyze the low-ionosphere response to an enhanced solar wind near Tromsø in the Arctic. Rodger et al. (1999) observed and explored the evolution regularity of ionospheric irregularity near the South Pole with the help of a riometer and HF radar. However, these studies were specific to different lays of the ionosphere and had limited geomagnetic conjugate

observations; thus, the similarities and differences of the ionospheric responses of the two hemispheres could not be analyzed because of the limited data from geomagnetic conjugate stations.

In the polar region, there are three Chinese overwinter research stations, with Zhongshan Station (ZHS) in Antarctica (69°22'24" S, 76°22'40" E) and Yellow River Station (YRS) in the Arctic (78°55'12" N, 11°55'48" E) located at approximately 75° Magnetic latitude(Mlat), 105° Magnetic longitude (Mlon) (ZHS: −74.77° Mlat, 97.77° Mlon; and YRS: 76.46° Mlat, 109.13° Mlon, CGM2012). Under quiet geomagnetic conditions, ZHS and YRS pass through the auroral zone twice a day and are located in the polar cusps near magnetic noon and the polar caps near magnetic midnight, which means that they have favorable geomagnetic latitudes for space physics observations in polar regions. At present, the ionospheric observation instruments deployed at ZHS include three-wavelength auroral imagers, an imaging riometer, an ionosphere total electron content (TEC) monitor, a Super Dual Auroral Radar Network (SuperDARN) HF coherent radar, and an ionosonde. The ionosphere observation instruments deployed at YRS include three- wavelength auroral imagers, an imaging riometer, an ionosphere TEC monitor, among others. The various observation approaches provide information from different perspectives on the variation characteristics of the ionosphere in polar regions, especially at cusp latitudes. A typical interplanetary shock event that affected the Earth space environment in July 2012 was studied. The analysis compared ionospheric observation data collected at ZHS and YRS to identify the similarities and differences of the ionosphere response process at the conjugate stations during this event and the discussion has been made to try to identify the energy transfer mechanisms with the different physical phenomena.

2 Interplanetary shock event on July 12–14, 2012

At 16:53 UT on July 12th, 2012, the sunspot group named AR1520 on the Sun's disk erupted an X1.4 sun flare when the sunspot group was directly facing the Earth. Subsequently, the coronal mass approached the magnetopause of the Earth at approximately 18:10 UT on July 14 (Cheng et al., 2014; Möstl et al., 2014).

An overview of the solar wind and IMF conditions is shown in Figures 1a–1e. The parameters shown are IMF components (a) B_x, (b) B_y, (c) B_z, (d) solar wind speed, and (e) solar wind dynamic pressure. Figures 1f and 1g present the temporal variations in the auroral electrojet (AE), amplitude upper (AU), amplitude lower (AL) and symmetric (SYM)-H indices, respectively. The data were extracted from NASA/GSFC's OMNI dataset with a 1 min time resolution through OMNIweb. Since the IMF and solar wind data in OMNI are given at the nose of the magnetopause, there should be some propagation time before an effect is seen in the ionosphere. This propagation time was estimated to be 2 min from the magnetopause to the ionosphere (Liou, 1998). In other words, the ionospheric response should be detected by ground observations later than 18:12 UT. It should be noted that not all the response times of the ionosphere were equal to this propagation time, especially the processes taking place in the magnetotail.

Figures 1e and 1f show that the interplanetary shock wave arrived at the nose of the magnetopause at approximately 18:10 UT on July 14, before which the solar wind dynamic pressure and IMF were both under quiet conditions. Within 2 min after 18:10 UT, the solar wind velocity suddenly increased from approximately 350 km·s^{-1} to 550 km·s^{-1}, and the solar wind dynamic pressure (illustrated in Figure 1f) ascended from 1 nPa to 5 nPa. Moreover, simultaneous sudden fluctuation occurred to the IMF components. The *By* component changed from approximately −3 nT to +10 nT, and the B_z component presented an obvious southward enhancement, shifting from approximately −3 nT to −13 nT. The solar wind dynamic pressure continued to increase up to 10 nPa, and the solar wind velocity was further accelerated to approximately 600 km·s^{-1}. These results implied that the studied event was a typical interplanetary shock event induced by the coronal mass ejection (CME).

As shown in Figure 1g, the level of the SYM-H index was relatively small before 18:10 UT. Then, at approximately 18:10, the SYM-H index abruptly increased from approximately 10 nT to 45 nT within 2 min. This phase appeared to be the sudden storm commencement (SSC). Afterwards, the initial phase of the geomagnetic storm began and lasted for approximately 7 h. During this period, the SYM-H index was hovering higher than that before the SSC and presented two peak-to-bottom variation cycles. At 18:50 UT on July 14, the maximum AE index occurred approximately with 1650 nT. During the aforementioned event, the B_z component of the IMF maintained its southward direction.

3 Instruments and data processing procedure for conjugate observations

At approximately 18:10 UT on July 14, 2012, the interplanetary shock wave reached the Earth's magnetopause, which disturbed the near-Earth space weather. The polar ionosphere presented a series of response. We managed to observe the response process of the polar ionosphere using ground-based conjugate observation platforms in the polar regions. Since the event occurred in July, for the geomagnetic conjugate polar observations at the two poles, ZHS in Antarctica was experiencing polar night, while YRS in the Arctic was in

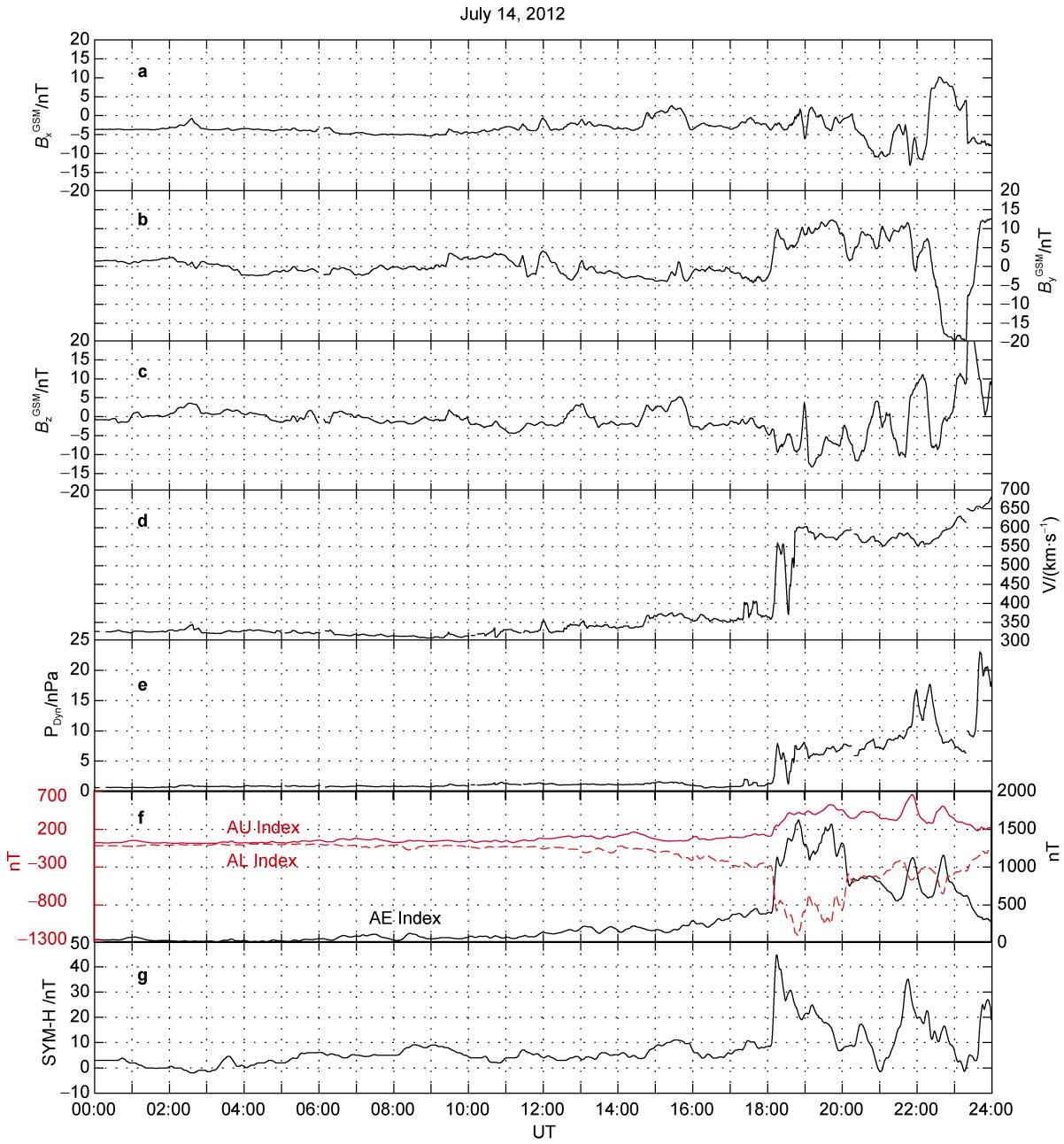

Figure 1 IMF and solar wind parameters, AE index, and SYM-H index on July 14, 2012: **a**, B_x; **b**, B_y; **c**, B_z; **d**, solar wind velocity; **e**, solar wind dynamic pressure; **f**, AE, AU and AL indices; and **g**, SYM-H index.

Table 1 Operating instruments for polar conjugate observation

Stations	Operating instruments		
	Three-wavelength aurora CCD imager (λ=630.0 nm/557.7 nm/427.8 nm)	Ionosphere TEC monitor	Imaging riometer
ZHS, Antarctica	√	√	√
YRS, Arctic	×	√	√

polar day. Because of the inappropriate light conditions, aurora observations were not performed in YRS. The conjugate observation instruments involved in this event are listed in Table 1.

3.1 Three-wavelength aurora CCD imager

The aurora observations at ZHS used an electron multiplier charge-coupled device (EM-CCD) equipped with a front

filter wheel to measure the auroral photoemissions intensity with three-wavelength of at 427.8, 557.7 and 630.0 nm in sequence (interferential filters centered at 427.8, 557.7 and 630.0 nm with a width of 2 nm, respectively). The front part of the imager was fixed with a fisheye lens to capture all-sky images above the horizon line. At a height of 150 km, the spatial resolution was ~36 km at the boundary of the field of view and ~1 km at the zenith. The azimuth of the all-sky imaging was calibrated using the fixed coordinates of the constellation, and the absolute intensity of the EM-CCD output was calibrated during fabrication (Hu et al., 2017).

The three-wavelength auroral intensity crossing the zenith along the geomagnetic north-south and east-west directions was extracted. The data were placed along the horizontal axis at positions that corresponded to the actual time of the observations. The time-sequence image of the auroral intensity along the geomagnetic meridian is called a keogram (Yang et al., 2000). It should be noted that the three-wavelength aurora observations could not obtain aurora images of the three wavelengths simultaneously because the aurora images of the three wavelengths were captured by rotating the filter wheel in sequence. Therefore, a keogram with a temporal resolution of 1 s was obtained via interpolations in the time domain. Moreover, as the zenith angle increased, the discrepancy between the auroral intensity captured in the all-sky image and the actual auroral illumination intensity grew. Accordingly, an aurora intensity correction factor was introduced in the image data processing procedure for calibration (Yang et al., 1997).

3.2 Imaging riometer

A set of imaging riometers was deployed at both ZHS and YRS, and they performed scanning every second through 8 × 8 = 64 antennas and recorded the voltage amplitude of the cosmic noise at 38.2 MHz and 38.235 MHz at ZHS and YRS, respectively. For the imaging riometer receiver at YRS, the 64 crossed dipoles were configured as a filled phased array; although the beam-forming process created 64 beams, not all of these were deemed usable. The postprocessing software normally used data from 49 beams (Honary et al, 2011). At ZHS, the 64 channels of the receiver signal were formed into 8 × 8 = 64 beams (Deng et al, 2005). The half-power width of the beam forming at a height of 90 km for the two imaging riometers at YRS and ZHS are shown in Figure 2.

A credible quiet day curve (QDC) of the cosmic noise is essential for determining the characteristics of the cosmic noise absorption, and the calculation of the QDC is dependent on the statistical computation of the receiving level of each beam of the antenna array under quiet geomagnetic conditions. Observation data from 15 days both before and after July 14 were used to derive the ionospheric QDCs applicable to that day for the two stations based on the QDC statistic algorithm (He et al., 2014); subsequently, the daily ionosphere absorption variation in each beam was calculated. With reference to the auroral keogram, the absorption data were then arranged as a keogram-type diagram of absorption intensity versus time.

3.3 Ionosphere TEC monitor

An ionospheric TEC monitor was deployed at both YRS and ZHS in 2010 and has been running continuously since then. The slant TEC value along multiple satellite-ground links at a specific moment was obtained by solving the ionospheric lag observation equation in real time (Chang et

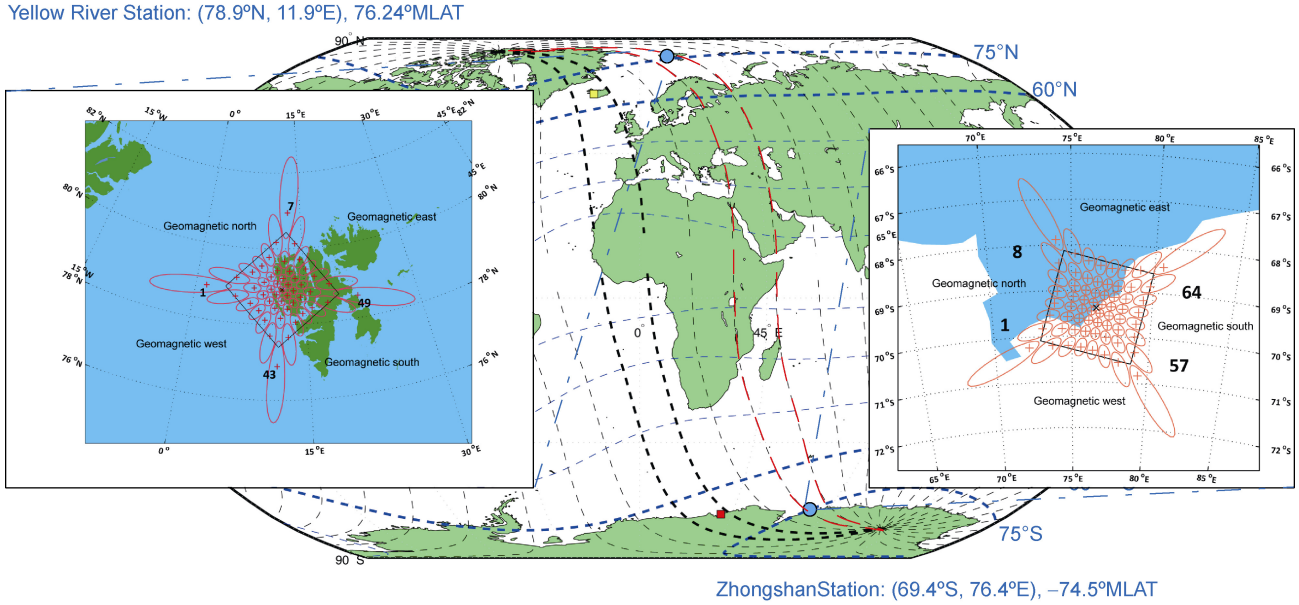

Figure 2 The projection of the half-power width of the antenna beams of the imaging riometer onto an ionospheric absorption altitude of 90 km at the Arctic YRS and the Antarctic ZHS.

al., 2001; Huang et al., 2003). The ionosphere TEC monitors generated the TEC data every 15 s, which included a date and time stamp, satellite reference number, slant TEC value, satellite azimuth and elevation angles.

To obtain the vertical TEC directly above the local observation station, slant TEC data with zenith angles less than 60° were selected for each sampling instant. Then, the vertical TEC for each satellite-ground receiver link was converted from the ionospheric slant TEC through the cosine projection function by the assumption of a unified 300 km height for the ionosphere pierce point of the satellite-ground links. The vertical TEC for all valid links was used to generate the vertical TEC value at the observation station using the modified Kriging interpolation method (Liu et al., 2008, 2011).

4 Conjugate observation results

Geomagnetically conjugate points can be calculated by field line tracing technique from a point in one hemisphere to the opposite hemisphere. In field line tracing for high-latitude stations, both the Earth's internal field and the external field caused by magnetospheric currents must be taken into consideration. The polar cap is a region of open field lines connected to the IMF. It seems difficult to define geomagnetic conjugate points in this region. However, if the invariant latitudes are not too high (less than ~77°) and the magnetic local times (MLTs) are far from the noon and midnight hours, geomagnetic conjugate points can be calculated using the Tsyganenko model (Yamagishi et al., 1998).

In our calculation, the Tsyganenko 2001 model (Tsyganenko, 2002a, 2002b) was used along with the GEOPACK library, which included subroutines for the International Geomagnetic Reference Field (IGRF) model, to find the conjugate points of ZHS in the Arctic. The Tsyganenko model input parameters of solar wind dynamic pressure and velocity, transverse components (B_y and B_z) of the IMF and Dst-index on July 14, 2012, were extracted from the websites https://cdaweb.gsfc.nasa.gov/index.html/ and http://wdc.kugi.kyoto-u.ac.jp at specific hours.

The daily drift traces of the conjugate point of ZHS on July 14th, 2012, are shown in Figure 3 as the red dashed lines. The red dots in the black circle show the conjugate position on the hour. It should be noted that at 11:00 UT and 12:00 UT, the Tsyganenko 2001 model showed that ZHS was located in the open field-line area; at 18:00 UT, the raytracing simulation showed that the field line reached more than 60 Re away from the Earth. The results were considered, as there were no certain conjugate points at the three full hours in Figure 3. At 20:00 UT, the conjugate point of ZHS was at 71.07°E, 48.69°W, which was located in the western part of Greenland and was not shown in Figure 3. The above results provided a good estimate of the drift of the conjugate regions when we analyzed the conjugate data in the polar cap.

The aurora intensity keograms of the three wavelengths (λ=630.0 nm, 557.7 nm and 427.8 nm) and ionospheric absorption keograms during 18:20:35–18:37:35 UT on July 14, 2012, are presented in Figure 4. The vertical axis direction of all the panels is from magnetic south (MS)

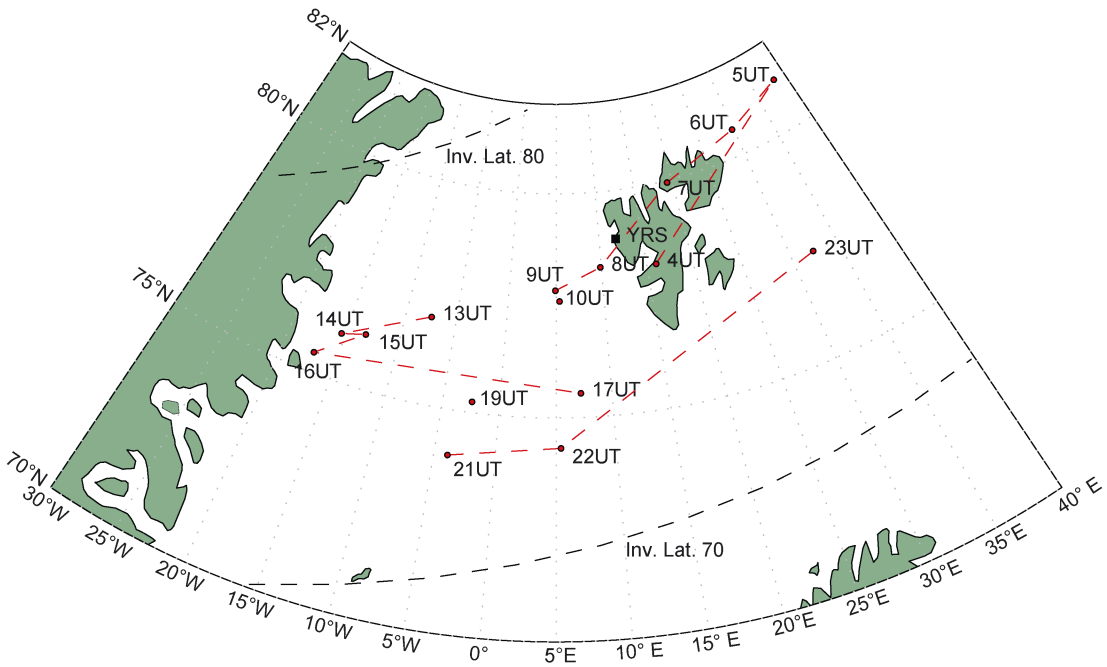

Figure 3 Daily drift motion of the conjugate point of Zhongshan Station on July 14, 2012.

to magnetic north (MN) along the magnetic meridian across the zenith in the center of the field of view. The keograms indicated the temporal and spatial developments of the aurora and ionospheric absorption horizontally along the MS-MN direction. The keograms of the auroral intensity for wavelengths of 630.0 nm, 557.7 nm and 427.8 nm are illustrated in Figures 4a, 4b and 4c, respectively. Figures 4d and 4e present keogram-type diagrams of the absorption intensities observed by the imaging riometers at ZHS and YRS, respectively. The Figure 4d presents the recorded data for the middle column of beams (i.e., beams 4, 11, 18, 25, 32, 39, and 46 from MN to MS), providing a central north-south cross section along with universal time. Similar to Figure 4, Figure 5 shows another set of keograms. The difference between Figures 4 and 5 is that the vertical axis of Figure 5 represents the direction across the zenith in the center of the field of view from magnetic east (ME) to magnetic west (MW) and indicates the development of the aurora and ionospheric absorption horizontally along the ME-MW direction.

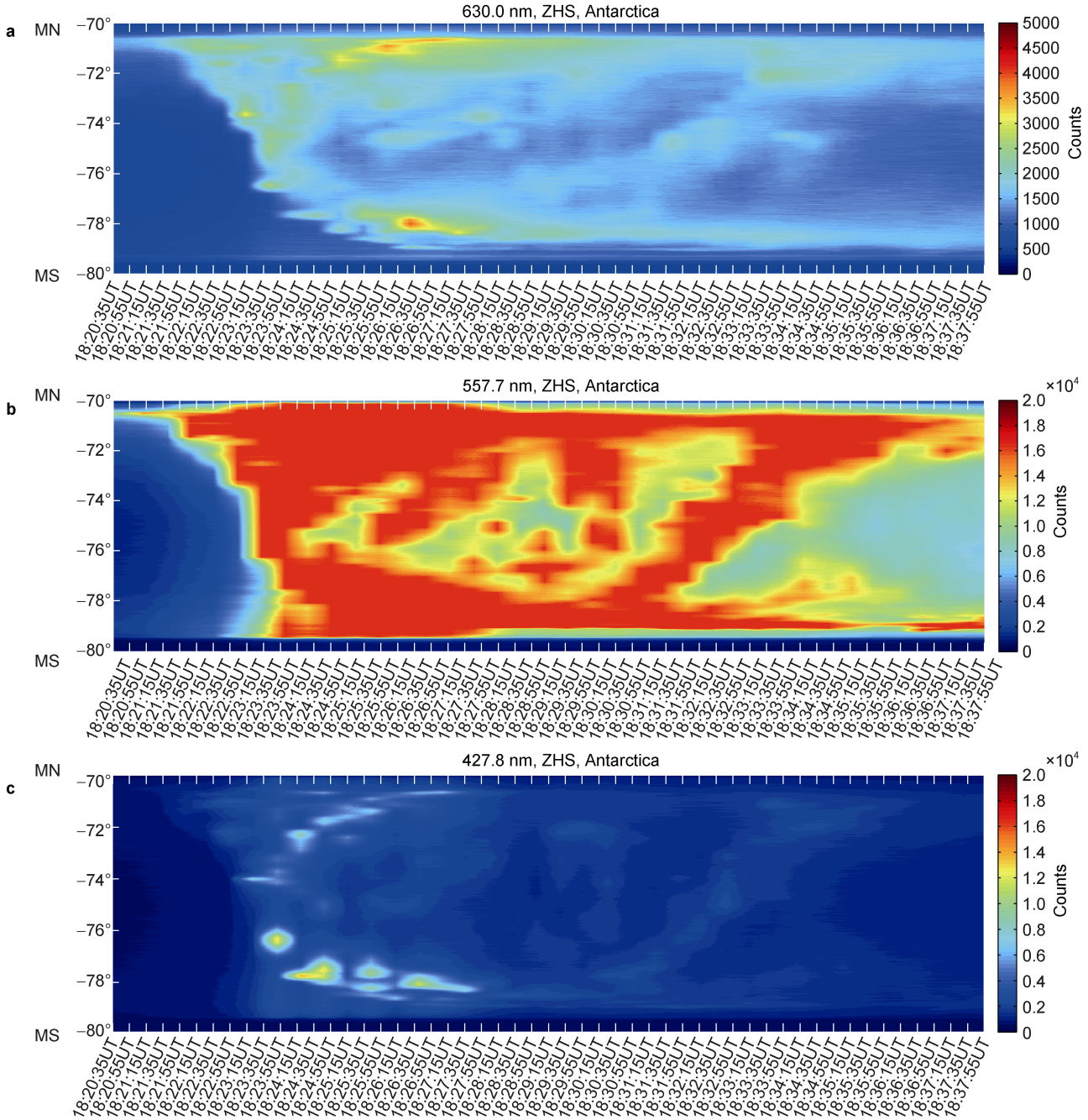

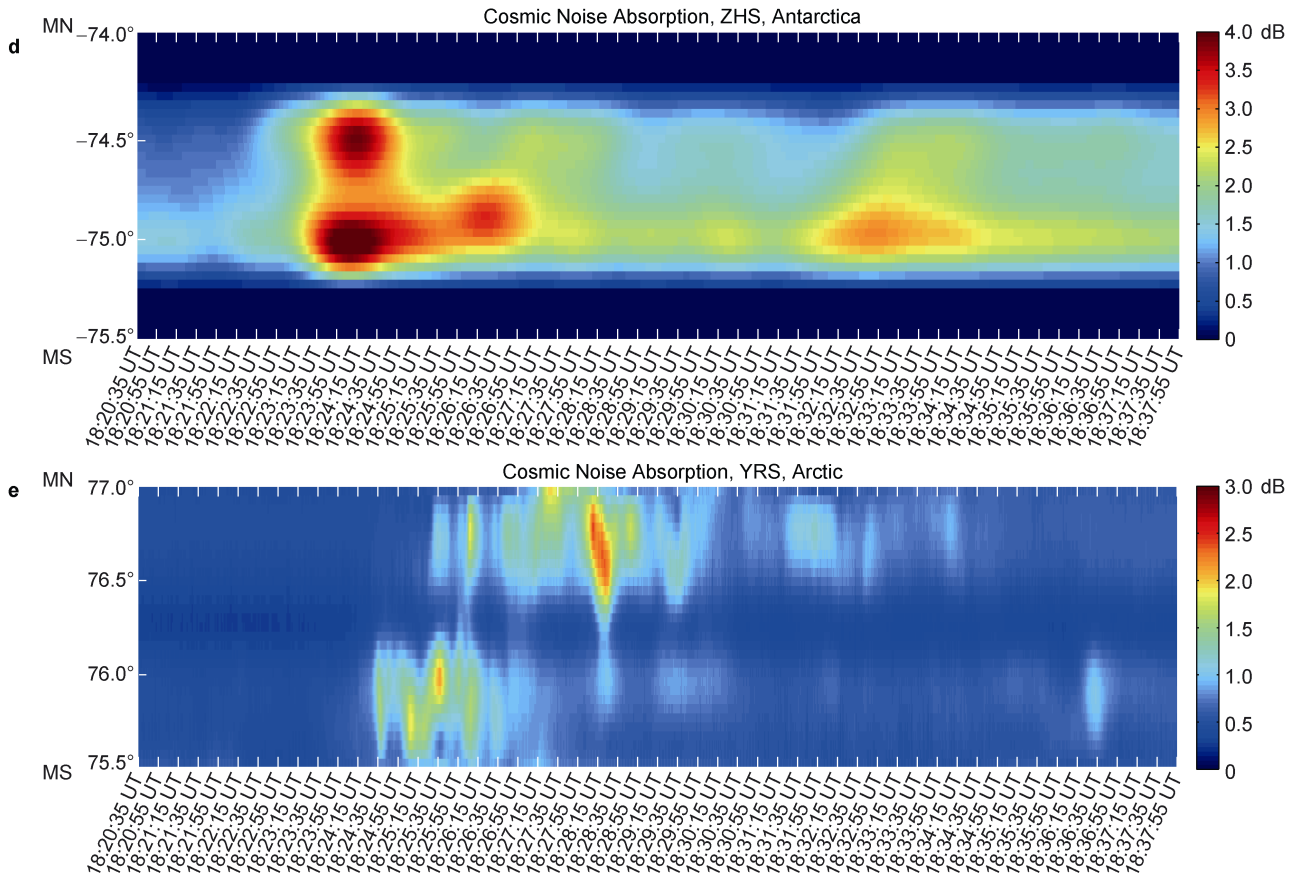

Figure 4 Keograms of the three-wavelength auroras (λ=630.0 nm, 557.7 nm and 427.8 nm) from 18:20:35~18:37:55 UT on July 14, 2012, at ZHS, Antarctica, and keograms of cosmic noise absorption from the same period at ZHS, Antarctica, and YRS, Arctic (along the geomagnetic south-north direction).

Figure 4 shows that the auroral onset at ZHS first appeared at the equatorward boundary within the field of view and was followed by a rapid poleward expansion, which was accompanied by a fast geomagnetic westward motion (Figure 5b). From 18:30 UT to 18:36 UT, part of the auroral arc broke up and presented poleward drifting, which was also exhibited fast geomagnetic eastward movement. Based on the three-wavelength aurora data, the highest auroral intensity occurred at the wavelength of 557.7 nm. This indicated that the precipitating electron flux, which caused the aurora at the 557.7 nm wavelength, significantly increased in the field of view during this period. The auroral evolution pattern in Figure 4 shows the expansion from low to high latitudes and its subsequent contraction. Following the sudden commencement, a substorm was triggered at relatively low latitudes. Then, the aurora presented a multi-arc structure along the ME-MW direction, and it subsequently evolved into a drape aurora structure. Finally, the aurora moved equatorward with a narrow arc remained.

Simultaneous observations by the imaging riometer at ZHS could yield the two-dimensional spatial variation in the ionospheric cosmic noise absorption in a relatively narrow field of view. The motion patterns of the absorption along the MS-MN direction during 18:20:35–18:37:35 UT are shown in Figure 4d, while those along the ME-MW direction are illustrated in Figure 5d. The initiation of the absorption enhancement (~18:23 UT) occurred three minutes after the onset of the aurora (~18:20 UT). This might be caused by the wider field of view of the ASI with a fisheye lens, which made the ASI be capable of detecting the aurora almost horizontally, but the imaging riometer has a smaller view of ~200 km × 200 km at an altitude of 90 km. With the aurora's equatorward movement out of the field of view during 18:30–18:37 UT in Figure 4b, the absorption area displayed similar equatorward motion during 18:31–18:35 UT and faded out of the field of view before 18:37 UT. Absorption was characterized by two "hot spot" areas, of which the one at higher latitudes moved equatorward (Figure 4d, 18:23–18: 27 UT) with fast westward movement (Figure 5d, 18:23–18: 25 UT).

Panel e in Figure 4 and panel e in Figure 5 show the absorption event at YRS, where the commencement was ~80 s later than that at ZHS. The absorption value reached its peak at approximately 18:28:00 UT, showing magnetic southwestward movement that lasted for ~30 s. The second absorption peak occurred at approximately 18:25:35 UT, showing northeastward movement that lasted for ~10 s.

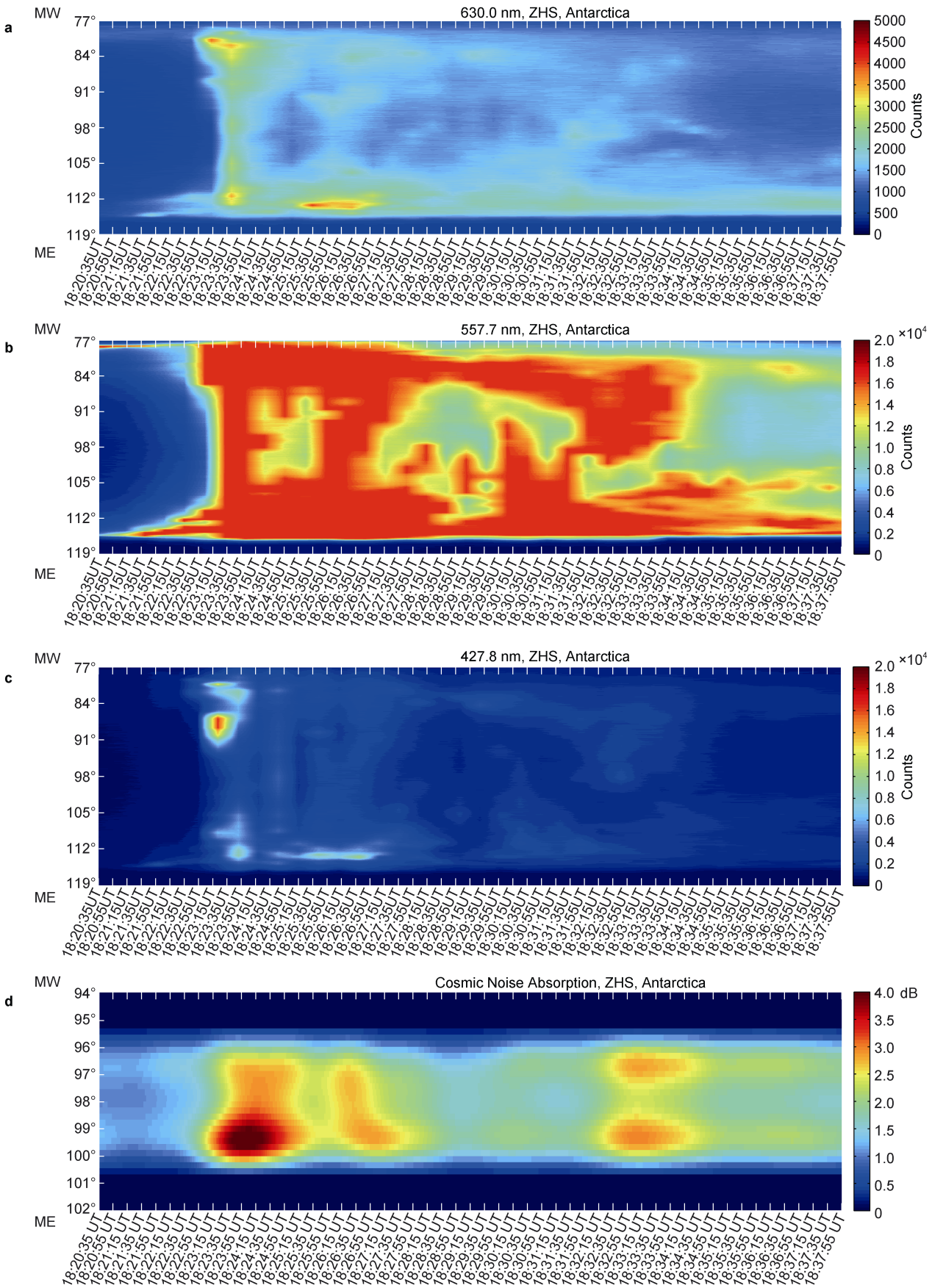
a
MW
630.0 nm, ZHS, Antarctica
77°
84°
91°
98°
105°
112°
119°
ME
5000
4500
4000
3500
3000
2500
2000
1500
1000
500
0
Counts
b
MW
557.7 nm, ZHS, Antarctica
77°
84°
91°
98°
105°
112°
119°
ME
×10^4
2.0
1.8
1.6
1.4
1.2
1.0
0.8
0.6
0.4
0.2
0
Counts
c
MW
427.8 nm, ZHS, Antarctica
77°
84°
91°
98°
105°
112°
119°
ME
×10^4
2.0
1.8
1.6
1.4
1.2
1.0
0.8
0.6
0.4
0.2
0
Counts
d
MW
Cosmic Noise Absorption, ZHS, Antarctica
94°
95°
96°
97°
98°
99°
100°
101°
102°
ME
4.0 dB
3.5
3.0
2.5
2.0
1.5
1.0
0.5
0

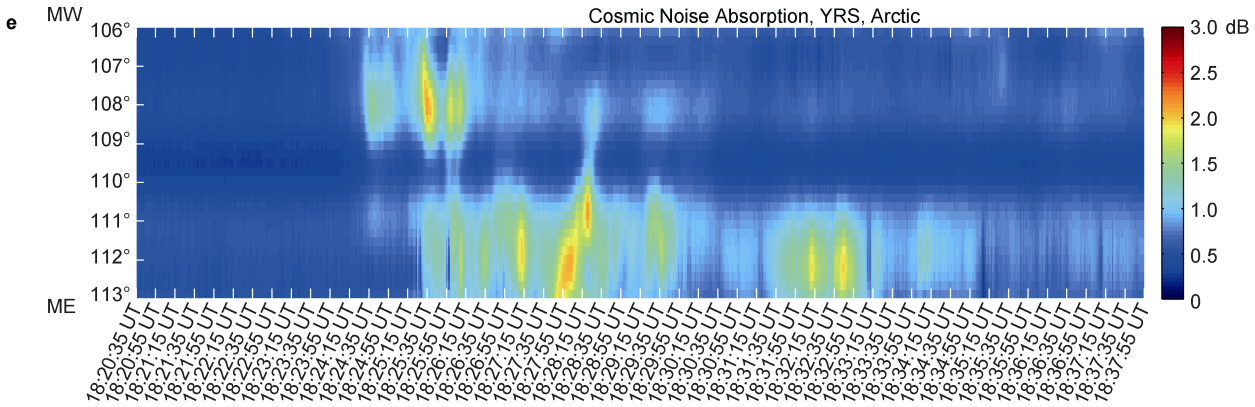

Figure 5 Keograms of the three-wavelength auroras (λ=630.0 nm, 557.7 nm and 427.8 nm) from 18:20:35–18:37:55 UT on July 14, 2012, at ZHS, Antarctica, and keograms of cosmic noise absorption from the same period at ZHS, Antarctica, and YRS, Arctic (along the geomagnetic east-west direction).

Aurora absorption is particularly well suitable for studies on the relative behaviors of auroral phenomena at magnetically conjugate points. Although one would expect to see the same intensity of absorption and the same patterns of variation, in fact, these expectations are rarely met. Based on panel d in Figure 4 and panel d in Figure 5, the nighttime absorption events at high latitudes exhibited temporal differences between the peaks of events in the conjugate regions, with the event that appeared first at ZHS being of greater intensity than its counterpart in the conjugate region at YRS. The absorption tended to be stronger at ZHS, which was in the winter hemisphere. These characteristics are consistent with the statistical features of absorption in conjugate regions proposed by Hargreaves and Cowley (1967).

5 Discussion

The studied interplanetary shock event occurred with a southward IMF enhancement, which may have caused an increase in the reconnection rate at the dayside magnetopause. The energy carried by solar wind was increasingly transferred to the magnetosphere and triggered the SSC and substorm.

Aurora absorption events were recorded simultaneously by riometers at both polar conjugate stations following the abrupt increases in the solar wind velocity and dynamic pressure along with the positive turning of the B_y component of the IMF. The absorption dynamic pattern recorded at ZHS displayed similar variation with that of the aurora forms (λ=557.7 nm) by the in situ aurora imager (initially moving equatorward and then poleward). However, the similarities between optical auroras and the cosmic noise absorption (CNA) at the auroral poleward boundary do not mean that the mechanism of both phenomena is the same because CNA is caused by the precipitation of electrons of several tens of keV, while optical auroras are caused by electrons of several keV. The absorption extension recorded at YRS was relatively small (Figure 4e), and the dynamic patterns displayed a local southwestward extension, which indicated anti-sunward movement. When the CNA is much greater than 1 dB, it is usually ascribed to the precipitation of electrons of several tens of keV. During poleward expansion, electrons in this energy range are produced by the reconnection process at a separatrix in the magnetotail. Some of these hot electrons precipitate directly into the polar ionosphere, causing CNA. The poleward progression of CNA bands could be explained by the continuous formation of a new separatrix just tailward of the preceding separatrix. The onset of the absorption event at ZHS occurred 80 s in advance of that at YRS, and both the absorption coverage and intensity at ZHS were greater than those at YRS. As shown in Figure 3, the model calculation showed that the raytracing simulation of the conjugate field line reached more than 60 Re away from the Earth, which means that there could be no certain conjugate point at approximately 18:00 UT. This implies that when the commencement of the substorm occurred, the two stations might not have been located in the same closed field line and might have been affected by separate reconnection processes at the magnetotail. Figure 3 also shows that the conjugate point of ZHS drifted around the Svalbard area at different times, which could also result in temporal differences in commencement between the two stations.

The TEC monitor takes the measurement of the total number of electrons along the radio wave propagation path integrated between global navigation satellite system (GNSS) satellites and the ground-based receiver with a tube with a cross section of one meter squared. During the polar night period, the variation in diurnal TEC profiles could be taken as an indicator of electron density change in the ionosphere caused by the effects of polar convection or particle precipitation. As both of the conjugate stations were deployed with the in situ TEC monitors, the TEC data were analyzed, and the vertical TEC over both stations was generated by applying the method presented in Section 3.3.

The vertical TEC variations at ZHS and YRS on July 14, 2012, were shown in Figures 6a and 6c (blue solid lines), respectively. The blue dashed lines presented the TEC diurnal variation on July 13, 2012, under quiet geomagnetic activity. The red solid lines were the TEC difference between the aforementioned two days, i.e., $\Delta TEC=TEC_{D14}-TEC_{D13}$, which indicated the TEC increase related to the interplanetary shock event. The ΔTEC variations during 18:00–19:00 UT at the two stations were illustrated in Figures 6b and 6d, respectively.

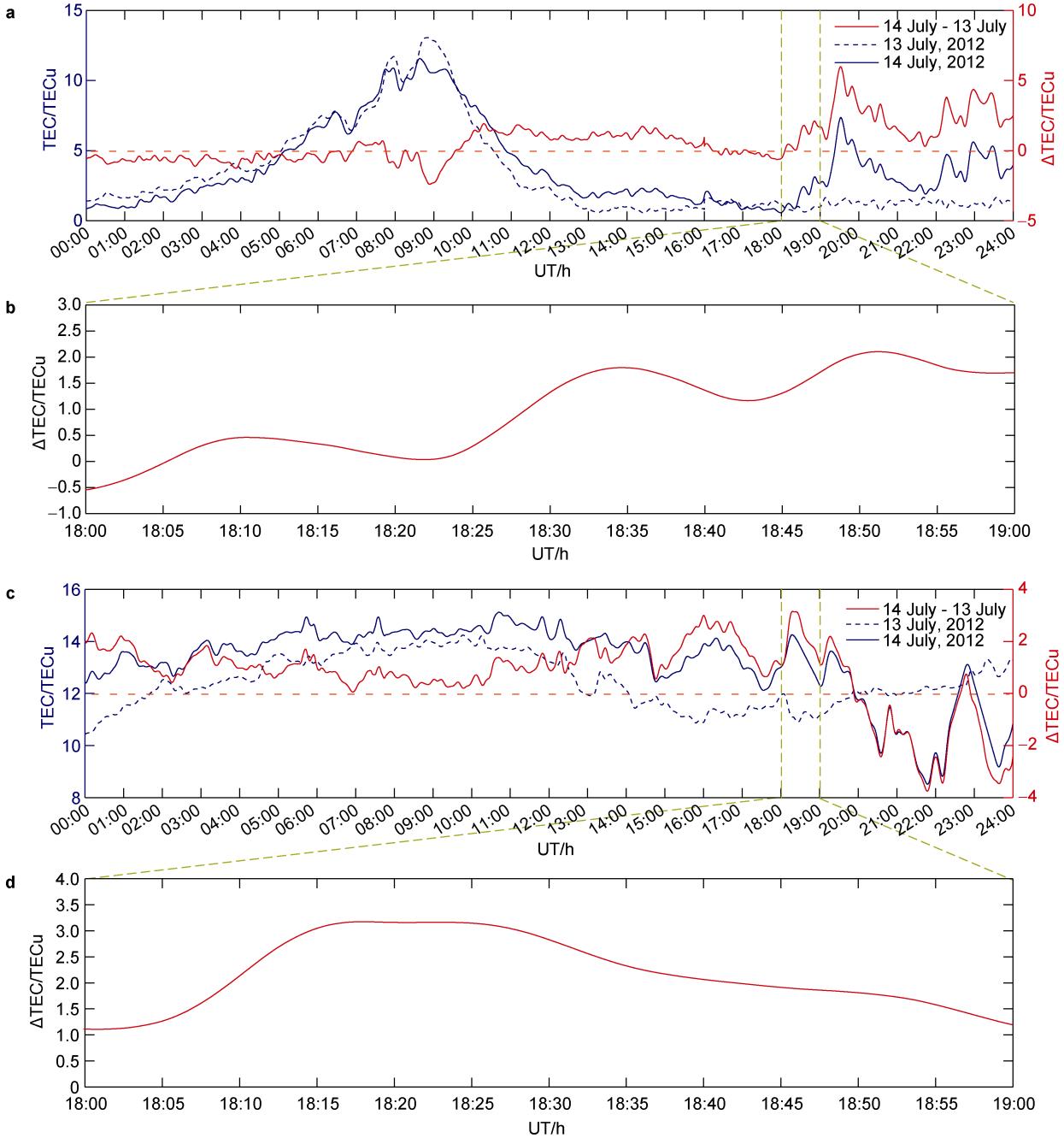

Figure 6 TEC observation results on July 14, 2012, at the polar conjugate stations: **a**, TEC at ZHS, 00:00–24:00 UT; **b**, ΔTEC at ZHS, 18:00–19:00 UT; **c**, TEC at YRS, 00:00–24:00 UT; and **d**, ΔTEC at YRS, 18:00–19:00 UT.

He et al. (2011) performed a statistical study on the foF2 seasonal features for the solar minimum year observed at ZHS. The diurnal variation in winter peaked at approximately 9:00 UT/10:50 MLT. Similarly, Figure 6a shows that the TEC variation above ZHS had its peak at approximately 9:00 UT. The fact that both the foF2 and TEC peaks occurred near magnetic noon (10:14 UT) meant that during the polar night, the ionosphere over ZHS at magnetic noon might have been affected by plasma drift induced by polar plasma convection, which led to an

increase in the electron density. It should be noted that the photoionization effects on the electron production of the ionosphere during the polar night were relatively weak and could be neglected. After 18:00 UT, compared with the case on July 13, the TEC showed a clear enhancement. The peak value at approximately 19:30 UT was less than the peak that occurred at 9:00 UT in Figure 6a. In terms of ΔTEC, compared with that on July 13 with quiet geomagnetic activity, its variation before 18:00 UT on July 14 was in a relatively small range, with a deviation of only approximately −2 TEC units (TECu) at approximately 9:00 UT. However, after 18:00 UT, the ΔTEC showed a continuous increase for the rest of the day, as shown in Figure 6a, and rapid positive growth of ΔTEC commenced at 18:23 UT. Comparison of the commencement times in Figures 4 and 5 demonstrates that the initiation of ΔTEC enhancement occurred simultaneously with the onset of the aurora appearance and with the ionosphere absorption intensification. Since this event occurred at austral polar night, the electrons generated by photoionization effects at the *F*-layer did not play a main part in the TEC composition. Moreover, the tongue of ionization (TOI) dragged by the anti-sunward convection on the dayside of the polar region was relatively weak during the polar night. The magnetic latitude of ZHS is 74.83°, and its location is shown in Figure 8 under polar convection patterns; this location was far from the anti-sunward convection area. This might have further reduced the possibility of TEC enhancement caused by plasma irregularities dragged by the anti-sunward convection, which is supported by Figure 8 in which there was no evident echo from irregularities over ZHS during the period. This implies that the ΔTEC enhancement might have been related to the electron density increase in the lower ionospheric layer induced by aurora particle precipitation.

Liu et al. (2017) presented polar ionosphere convection patterns during the period of this event. They were plotted by the map potential fitting method (Ruohoniemi and Baker, 1998) using SuperDARN (Greenwald et al., 1995) data. The patterns of the Northern and Southern Hemispheres are shown in Figures 7 and 8, respectively, and the locations of the two conjugate stations, i.e., YRS and ZHS, are marked. The sounding range of the Hankasalmi radar in the Arctic and the Kerguelen radar in Antarctica cover the area over YRS and ZHS, respectively, and the line-of-sight velocity of the irregularity drift over the two stations is also shown along with the convection patterns.

In Figure 7a, at approximately 17:50 UT, the echo of the Hankasalmi radar almost appeared within the range gate of 1500 km, with no echo recorded over YRS. In Figure 7c, at approximately 18:10 UT, the ionosphere irregularity over YRS presented a movement toward the radar with a line-of-sight velocity of 125 $m \cdot s^{-1}$, and at approximately 18:30 UT in Figure 6e, i.e., 20 min after the initiation of the substorm expansion phase, the echo over YRS intensified. Beam 8 of the Hankasalmi radar always covers the location of YRS. The backscatter echo intensity of the beam during 17:50 to 19:00 UT is presented in Figure 9. This result indicated that the irregularities over YRS moved equatorward with a velocity of 150 $m \cdot s^{-1}$ or more from 18:32 to 18:56 UT, as marked by the dashed line.

For the other conjugate pair, ZHS in Antarctica, during 17:50–19:05 UT, the echo of the Kerguelen radar was sounded only within the slant range of 1000 km near the radar site, and no echo was sounded over or near ZHS, as shown in Figure 8. The backscatter echo intensity of beam 6 of the Kerguelen radar, which covered the area above ZHS, as shown in Figure 10, also showed the same feature. This might be caused by (1) reduced photoionization effects during the polar night and the consequent reduction in *F*-layer electron density and (2) weakened anti-sunward convection with suppressed formation of a TOI during the polar night, which reduced the occurrence of backscatter echoes from ionospheric plasma irregularities over ZHS.

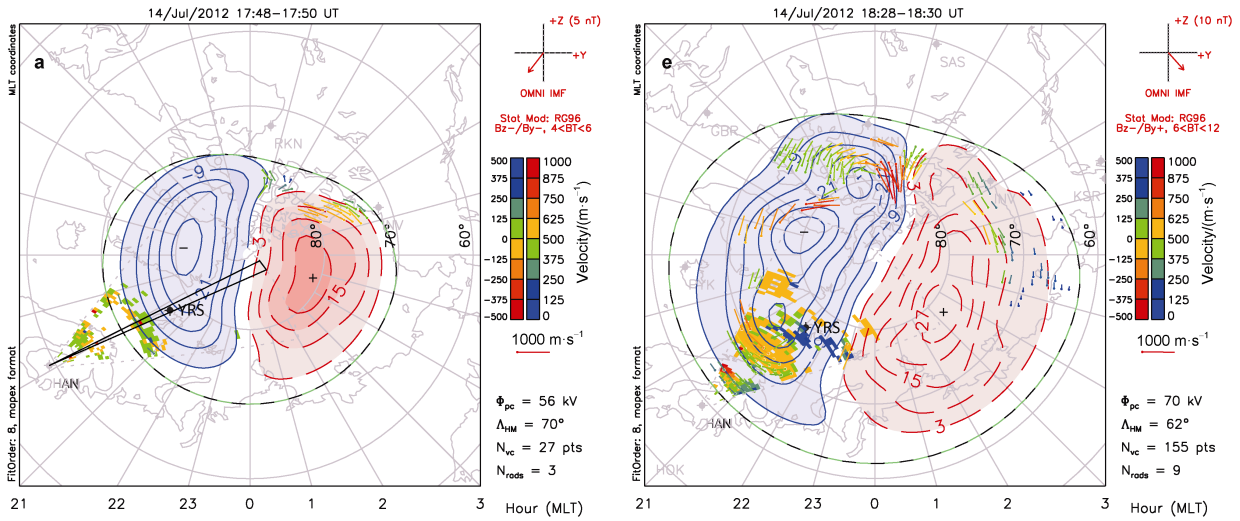

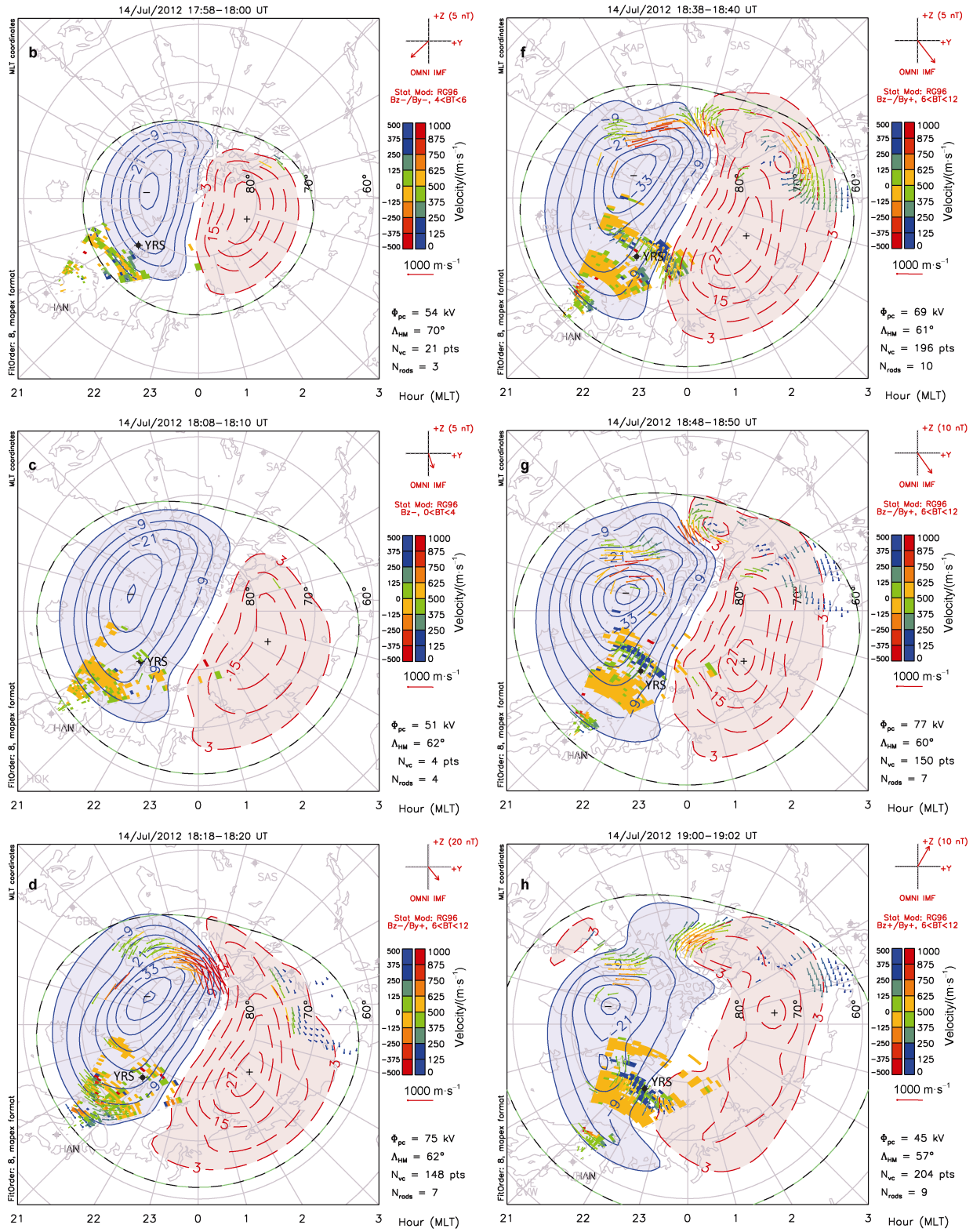

Figure 7 Doppler line-of-sight velocity of the irregularities observed by the Arctic Hankasalmi HF radar and ionospheric convection observed by SuperDARN from 17:50–19:00 UT on July 14, 2012 (● indicates the location of YRS; red and blue dashed lines represent the potential contour of the polar cap on the dawn and dusk sides, respectively; the outside blue dashed line refers to the boundary of the ionospheric convection; the left color bar corresponds to the Doppler line-of-sight velocity of irregularities; the right color bar stands for the convection velocity; and beam 8, which covers YRS, is outlined in black dashes in panel **a**).

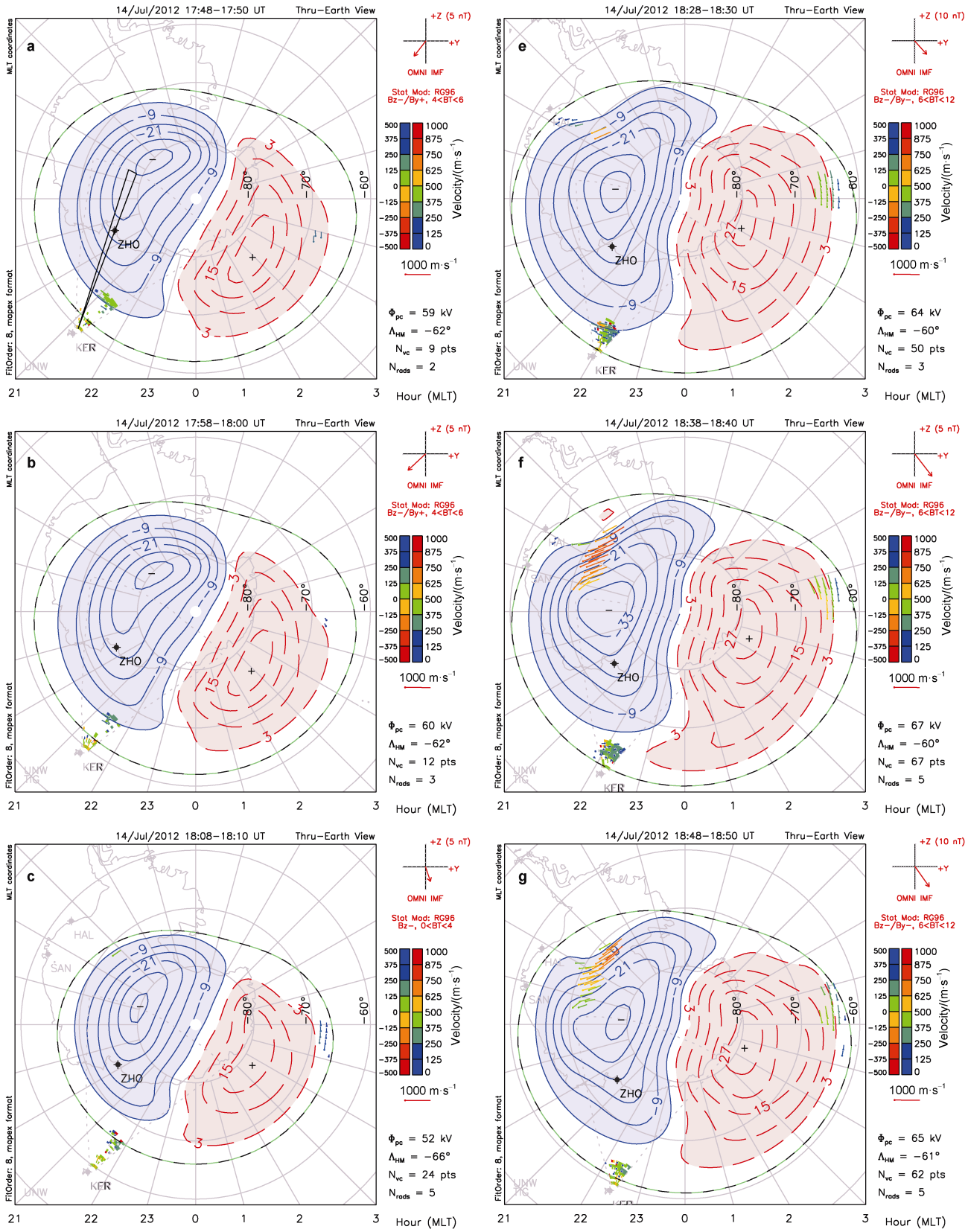
a
14/Jul/2012 17:48–17:50 UT
Thru–Earth View
+Z (5 nT)
+Y
OMNI IMF
Stat Mod: RG96
Bz–/By+, 4<BT<6
Velocity/(m·s⁻¹)
1000 m·s⁻¹
Φpc = 59 kV
ΛHM = −62°
Nvc = 9 pts
Nrods = 2
MLT coordinates
FitOrder: 8, mapex format
ZHO
KER
UNW
Hour (MLT)
b
14/Jul/2012 17:58–18:00 UT
Thru–Earth View
Stat Mod: RG96
Bz–/By+, 4<BT<6
Φpc = 60 kV
ΛHM = −62°
Nvc = 12 pts
Nrods = 3
c
14/Jul/2012 18:08–18:10 UT
Thru–Earth View
Stat Mod: RG96
Bz–, 0<BT<4
Φpc = 52 kV
ΛHM = −66°
Nvc = 24 pts
Nrods = 5
HAL
SAN
e
14/Jul/2012 18:28–18:30 UT
Thru–Earth View
+Z (10 nT)
Stat Mod: RG96
Bz–/By–, 6<BT<12
Φpc = 64 kV
ΛHM = −60°
Nvc = 50 pts
Nrods = 3
f
14/Jul/2012 18:38–18:40 UT
Thru–Earth View
Stat Mod: RG96
Bz–/By–, 6<BT<12
Φpc = 67 kV
ΛHM = −60°
Nvc = 67 pts
Nrods = 5
PG
g
14/Jul/2012 18:48–18:50 UT
Thru–Earth View
Stat Mod: RG96
Bz–/By–, 6<BT<12
Φpc = 65 kV
ΛHM = −61°
Nvc = 62 pts
Nrods = 5

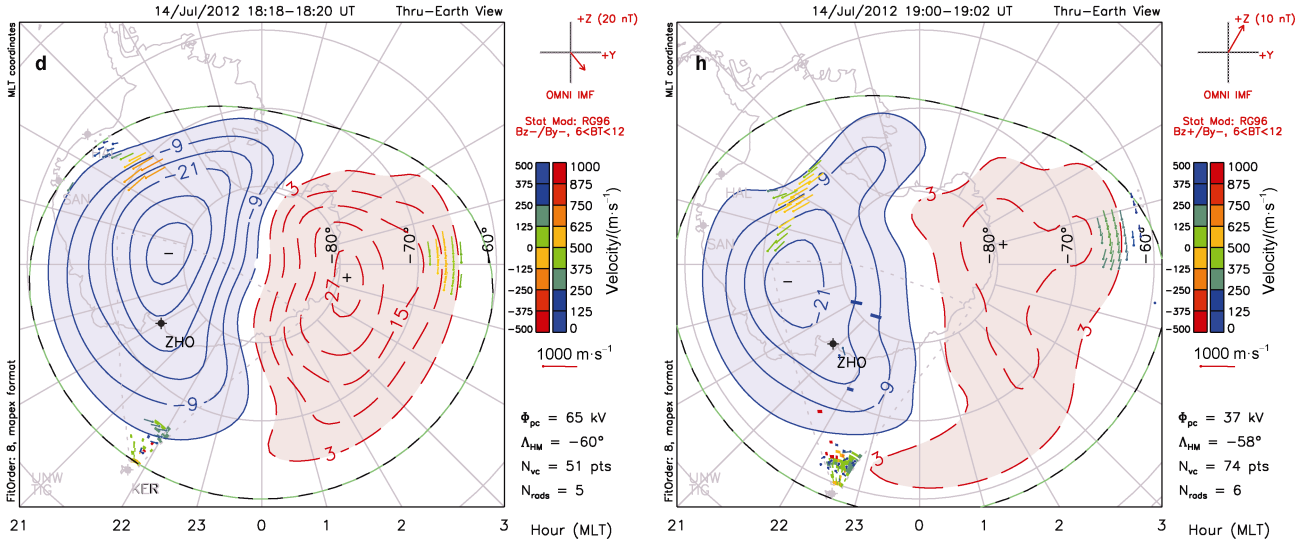

Figure 8 Doppler line-of-sight velocity of the irregularities observed by the Antarctic Kerguelen HF radar and ionospheric convection observed by SuperDARN from 17:50–19:00 UT on July 14, 2012 (● indicates the location of ZHS; red and blue dashed lines represent the potential contour of the polar cap on the dawn and dusk sides, respectively; the outside blue dashed line refers to the boundary of the ionospheric convection; the left color bar corresponds to the Doppler line-of-sight velocity of irregularities; the right color bar stands for the convection velocity; and beam 6, which covers ZHS, is outlined in black dashes in panel **a**).

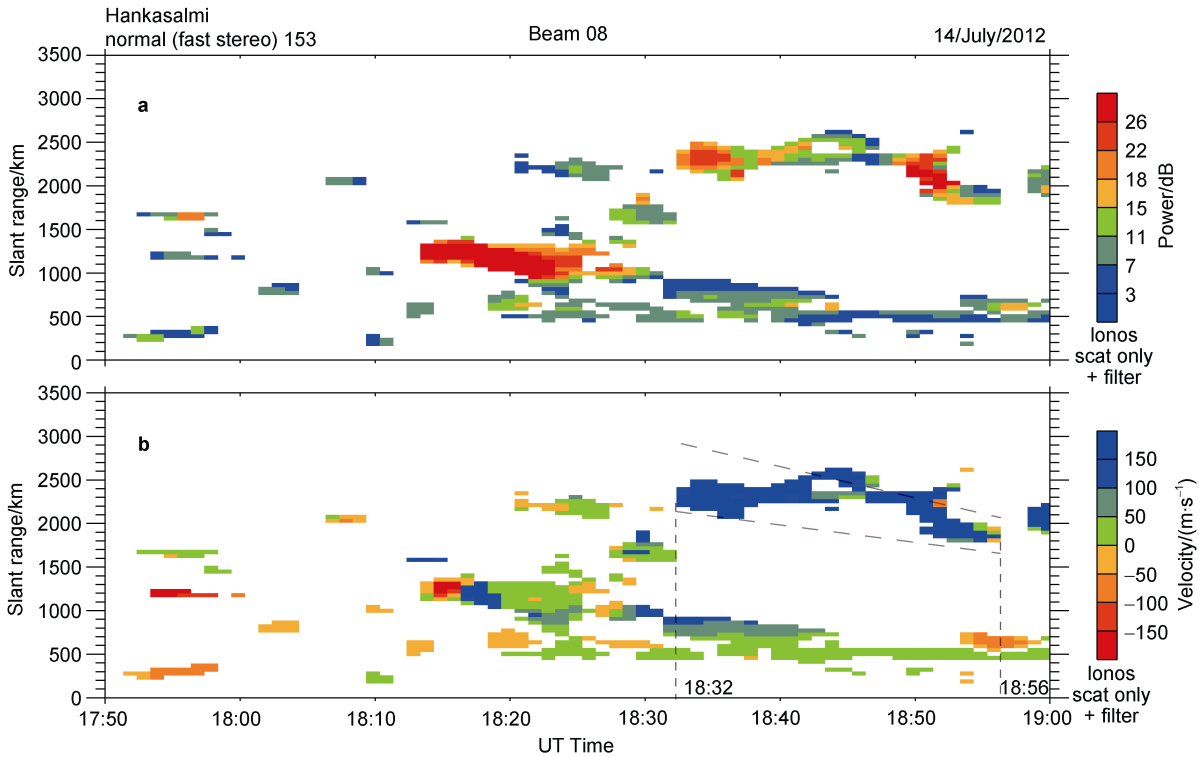

Figure 9 Backscatter echo intensity (**a**) and line-of-sight velocity (**b**) of the ionospheric irregularities measured by the 8th beam of the Arctic Hankasalmi HF radar from 17:50–19:00 UT on July 14, 2012.

In terms of YRS, the TEC stayed at a relatively high level of greater than 12 TECu and presented smaller variations before 18:00 UT than that of ZHS (Figure 6), and its diurnal TEC discrepancy was within 4 TECu. YRS was in the polar day in July, and the electron density in the *F*-layer generated by the photoionization effects was constantly maintained at a high level. Compared with the TEC data on the magnetically quiet day of July 13, the TEC on July 14 showed a similar variation trend before 12:00 UT but with a higher value. The TEC presented a sudden

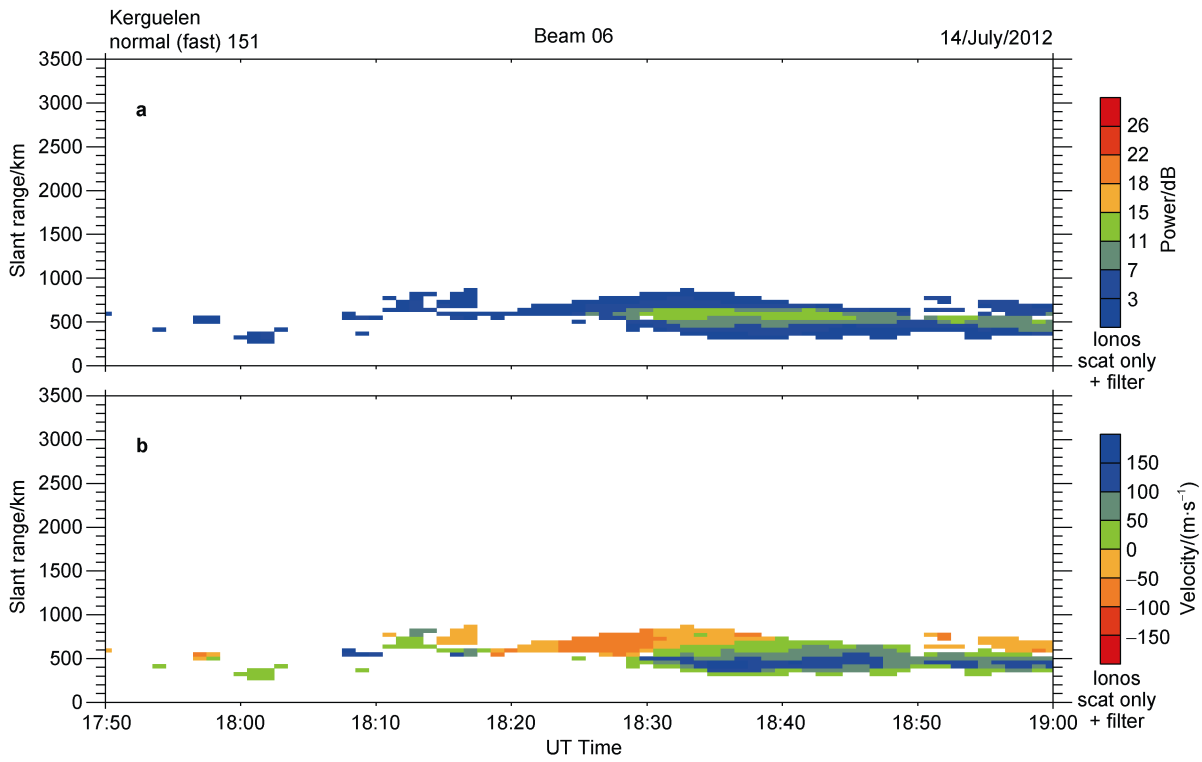

Figure 10 Backscatter echo intensity (**a**) and line-of-sight velocity (**b**) of the ionospheric irregularities measured by the 6th beam of the Antarctic Kerguelen HF radar from 17:50–19:00 UT on July 14, 2012.

increase of approximately 3 TECu just after 18:00 UT. Another increase in TEC occurred after 19:00 UT, with a magnitude of approximately 2 TECu. However, the TEC on July 14 rapidly declined to values below those on July 13 after 20:00 UT, and only a small recovery occurred at approximately 23:00 UT. Because YRS stayed in the polar day during this event, photoionization had dominant effects on the generation of electrons in the ionosphere. Figure 7 shows the ionospheric convection patterns over YRS during 18:00–19:00 on July 14, 2012, along with the location of YRS. With the development of the expansion phase of the substorm, YRS moved into the nightside reverse area of anti-sunward convection. By taking into account Figure 7c, at approximately 18:10 UT on July 14, the echo over YRS notably increased. This signified a strong anti-sunward plasma drifting. The TEC enhancement over YRS might have contributed to the enhancement of ionosphere irregularities along with anti-sunward convection across the polar cap region passing over YRS. The ionosphere absorption above YRS shown in Figure 4e presented magnetic southward movement within the short period from 18:27–19:29 UT. This motion might be caused by the effects of particle precipitation accompanied by the equatorward expansion of the aurora oval during the expansion phase of the substorm. The combination of particle precipitation and ionospheric irregularity movement could have led to the significant enhancement in the TEC over YRS.

The irregularities observed by the Hankasalmi radar over YRS were supposed to originate from the dayside by the photoionization effects and dragged by the convection to the nightside. The electron density was higher than the background, so it might have increased the CNA observed at YRS to a certain extent. The precipitated electrons from the magnetotail released by the substorm (tens of keV) likely enhanced the collision frequency of electrons in the lower ionosphere, which increased the CNA as well.

The different responses of the CNA to the nightside substorms in both hemispheres might have been caused by the fact that the two stations might not have been located in the same closed field line and were potentially affected by separate reconnection processes at the magnetotail when the commencement of the substorm occurred. The conductance over YRS was supposed to be higher than that of ZHS because YRS was in polar day and ZHS was in polar night. The photoionization effect can lead to an increased field-aligned current, which can lead to an enhanced precipitation electron flux. This is expected to result in a higher CNA over YRS than ZHS. However, the data showed the opposite conditions. This means that the origins of the CNAs over the two stations were different.

6 Conclusions

After the interplanetary shock event on July 14, 2012, that impacted the Earth-space environment, simultaneous observations of aurora evolution and ionospheric response

were observed by multiple instruments at geomagnetic conjugate stations in Antarctica, ZHS, and the Arctic, YRS. The ionosphere absorption, TEC, HF coherent radar backscatter echo and three-wavelength aurora form data in the polar region during the event were analyzed. The following conclusions were drawn.

(1) During the event period of 18:00–19:00 UT, the ionosphere absorption over YRS was weaker than that over ZHS, but the plasma irregularity echo was stronger. Local TEC enhancement could probably be induced by the passing of the ionosphere irregularity along the anti-sunward convection over YRS.

(2) The ionosphere absorption over ZHS was stronger than that over YRS, and significant aurora evolution was observed simultaneously. However, the in situ plasma irregularity drift was not obvious from the coherent HF radar data. The local TEC enhancement was mainly caused by aurora or energetic particle precipitation induced by the nightside substorm, which was triggered by this shock event.

(3) During this event, because of the higher geomagnetic latitude, the ionosphere over YRS was more severely affected by anti-sunward convection than that over the Antarctic ZHS. Moreover, YRS remained in the polar day during the event, and the TOI caused by both photoionization effects and polar convection was considerable, which led to the enhanced echo of the in situ ionospheric irregularity drift over YRS. However, the location of ZHS was far from the anti-sunward convection area. In addition, the ZHS was in polar night during the event. Because of the weak photoionization effects, the *F*-layer electron density was low, and the irregularity drift effects carried by polar convection were negligible. This probably caused the different echo observation results at the two conjugate stations.

(4) Geomagnetic conjugate observation stations could present various ionospheric responses to identical interplanetary shock events due to opposite photoionization conditions and different locations under polar convection patterns. Such differences would be notable in solstice seasons. The daily drift motion of the conjugate point and the mismatch of the conjugate pair might be another factor causing the different ionospheric responses. However, this weight factor would be evaluated more easily in equinox seasons.

The observation results also implied that the ionospheric response processes at different altitudes may have originated from the same electron precipitation source area in the magnetosphere. The temporal discrepancy in the response commencement at different altitudes may be attributed to the different particle acceleration mechanisms in the magnetosphere. The ionosphere absorption at the two conjugate stations presented similar variation characteristics, which were likely triggered by the same particle acceleration process in the magnetotail.

Acknowledgments This work was supported by the National Key R&D Program of China (Grant no. 2018YFF01013706), the National Natural Science Foundation of China (Grant no. 41831072) and the Top-Notch Young Talents Program of China (Grant no. W02070249). We acknowledge the use of NASA/GSFC's Space Physics Data Facility's CDAweb service, OMNI data and geomagnetic data provided by the World Data Center for Geomagnetism. We also acknowledge the use of data from the Chinese Meridian Project. We would like to thank the two anonymous reviewers and Associate Editor, Dr. Beichen Zhang for their valuable suggestions and comments regarding further improvement of this article.

References

Belon A E, Maggs J E, Davis T N, et al. 1969. Conjugacy of visual auroras during magnetically quiet periods. J Geophys Res, 74(1): 1-28, doi:10.1029/ja074i001p00001.

Chang Q, Zhang D H, Xiao Z, et al. 2001. Estimation method of GPS instrumental biases and its application in the calculation of TEC. Chin J Geophys, 44(5): 588-594, doi:10.1002/cjg2.178.

Cheng X, Ding M D, Zhang J, et al. 2014. Formation of a double-decker magnetic flux rope in the sigmoidal solar active region 11520. Astrophys J, 789(2): 93, doi:10.1088/0004-637x/789/2/93.

Deng Z X, Liu R Y, Zhao Z Y, et al. 2005. Polar ionospheric absorptions during solar storms at the end of October, 2003. Chin J Polar Res, 17(1): 23-31 (in Chinese with English abstract).

DeWitt R N. 1962. The occurrence of aurora in geomagnetically conjugate areas. J Geophys Res, 67(4): 1347-1352, doi:10.1029/jz067i004p01347.

Greenwald R A, Baker K B, Ruohoniemi J M, et al. 1990. Simultaneous conjugate observations of dynamic variations in high-latitude dayside convection due to changes in IMF B_y. J Geophys Res: Space Phys, 95(A6): 8057-8072, doi:10.1029/JA095iA06p08057.

Greenwald R A, Baker K B, Dudeney J R, et al. 1995. DARN/SuperDARN. Space Sci Rev, 71(1-4): 761-796, doi:10.1007/BF00751350.

Hargreaves J K, Cowley F C. 1967. Studies of auroral radio absorption events at three magnetic latitudes II: Differences between conjugate regions. Planet Space Sci, 15(10): 1585-1597, doi:10.1016/0032-0633(67)90091-8.

Hargreaves J K, Birch M J, Bromage B J I. 2007. *D*- and *E*-region effects in the auroral zone during a moderately active 24-h period in July 2005. Ann Geophys, 25(8): 1837-1849, doi:10.5194/angeo-25-1837-2007.

He F, Hu H Q, Hu Z J, et al. 2014. A new technique for deriving the quiet day curve from imaging riometer data at Zhongshan Station, Antarctic. Sci China Technol Sci, 57(10): 1967-1976. doi,10.1007/s11431-014-5616-z.

He F, Zhang B C, Joran M, et al. 2011. A conjugate study of the polar ionospheric *F*2-layer and IRI-2007 at 75° magnetic latitude for solar minimum. Adv Polar Sci, 22: 175-183, doi:10.3724/SP.J.1085.2011.00175.

Honary F, Marple S R, Barratt K, et al. 2011. Digital beam-forming imaging riometer systems. Rev Sci Instrum, 82(3): 031301, doi:10.1063/1.3567309.

Hu Z J, He F, Liu J J, et al. 2017. Multi-wavelength and multi-scale aurora observations at the Chinese Zhongshan Station in Antarctica. Polar Sci,

14: 1-8, doi:10.1016/j.polar.2017.09.001.

Huang Z, Yuan H, Wan W X. 2003. Test of GPS TEC hardware biases estimating methods. Chin J Radio Sci, 18(4): 472-476, doi:10.13443/j.cjors.2003.04.026 (in Chinese with English abstract).

Liou K, Newell P T, Meng C I, et al. 1998. Characteristics of the solar wind controlled auroral emissions. J Geophys Res: Space Phys, 103(A8): 17543-17557, doi:10.1029/98JA01388.

Liu R Y, Liu G H, Wu J, et al. 2008. Ionospheric f_0F_2 reconstruction and its application to the short-term forecasting in China region. Chin J Geophys, 51(2): 206-213, doi:10.1002/cjg2.1212 (in Chinese with English abstract).

Liu R Y, Wang J P, Wu Y W, et al. 2011. Method for short-term forecasting of ionospheric total electron content in Chinese region. Chin J Radio Sci, 26(1): 18-24, doi:10.13443/j.cjors.2011.01.008 (in Chinese with English abstract).

Liu Q Q, Hu H Q, Lv J Y, et al. 2017. Case study on nightside polar ionospheric convection response to interplanetary shock. Chin J Space Sci, 37(2): 140-150, doi:10.11728/cjss2017.02.140 (in Chinese with English abstract).

Martinis C R, Macinnis R, Sullivan C, et al. 2014. Ionospheric studies from low to sub-auroral latitudes using geomagnetic conjugate all-sky imagers and satellite data. AGU fall meeting 2014, San Francisco, CA, United States.

Möstl C, Amla K, Hall J R, et al. 2014. Connecting speeds, directions and arrival times of 22 coronal mass ejections from the Sun to 1 AU. Astrophys J, 787(2): 119, doi:10.1088/0004-637x/787/2/119.

Østgaard N, Mende S B, Frey H U, et al. 2004. Interplanetary magnetic field control of the location of substorm onset and auroral features in the conjugate hemispheres. J Geophys Res: Space Phys, 109(A7): A07204, doi:10.1029/2003JA010370.

Rodger A S, Rosenberg T J. 1999. Riometer and HF radar signatures of polar patches. Radio Sci, 34(2): 501-508, doi:10.1029/1998RS900005.

Ruohoniemi J M, Baker K B. 1998. Large-scale imaging of high-latitude convection with Super Dual Auroral Radar Network HF radar observations. J Geophys Res: Space Phys, 103(A9): 20797-20811, doi:10.1029/98JA01288.

Sato N, Nagaoka T, Hashimoto K, et al. 1998. Conjugacy of isolated auroral arcs and nonconjugate auroral breakups. J Geophys Res: Space Phys, 103(A6): 11641-11652, doi:10.1029/98JA00461.

Shand B A, Yeoman T K, Lewis R V, et al. 1998. Interhemispheric contrasts in the ionospheric convection response to changes in the interplanetary magnetic field and substorm activity: a case-study. Ann Geophys, 16(7): 764-774, doi:10.1007/s00585-998-0764-8.

Stenbaek-Nielsen H C, Davis T N, Glass N W. 1972. Relative motion of auroral conjugate points during substorms. J Geophys Res, 77(10): 1844-1858, doi:10.1029/ja077i010p01844.

Stenbaek-Nielsen H C, Otto A. 1997. Conjugate auroras and the interplanetary magnetic field. J Geophys Res: Space Phys, 102(A2): 2223-2232, doi:10.1029/96JA03563.

Stenbaek-Nielsen H C, Wescott E M, Davis T N, et al. 1973. Differences in auroral intensity at conjugate points. J Geophys Res, 78(4): 659-671, doi:10.1029/JA078i004p00659.

Tsyganenko N A. 2002a. A model of the near magnetosphere with a dawn-dusk asymmetry 1. Mathematical structure. J Geophys Res, 107(A8): SMP12-1, doi:10.1029/2001ja000219.

Tsyganenko N A. 2002b. A model of the near magnetosphere with a dawn-dusk asymmetry 2. Parameterization and fitting to observations. J Geophys Res: Space Phys, 107(A8): SMP10-1, doi:10.1029/2001JA 000220.

Wescott E M. 1966. Magnetoconjugate phenomena. Space Sci Rev, 5(4): 507-561, doi:10.1007/BF00240576.

Yamagishi H, Fujita Y, Sato N, et al. 1998. Conjugate features of auroras observed by TV cameras and imaging riometers at auroral zone and polar cap conjugate-pair stations//Moen J, et al. Polar Boundary Phenomena. Kluwer Academic Publishers.

Yang H G, Liu R Y, Natsuo S. 1997. Intensity correction in all-sky auroral image projection transform. Chin Sci Bull, 42(8): 700-703, doi:10.1007/BF03182656.

Yang H, Sato N, Makita K, et al. 2000. Synoptic observations of auroras along the postnoon oval: a survey with all-sky TV observations at Zhongshan, Antarctica. J Atmos Sol Terr Phys, 62(9): 787-797, doi:10.1016/S1364-6826(00)00054-7.

Yeoman T K, Lewis R V, Milan S E, et al. 1999. An interhemispheric study of the ground magnetic and ionospheric electric fields during the substorm growth phase and expansion phase onset. J Geophys Res: Space Phys, 104(A7): 14867-14877, doi:10.1029/1999JA900164.

Supplementary Figures

The 2D images of CNA and aurora over ZHS are shown as Supplementary Figures below:

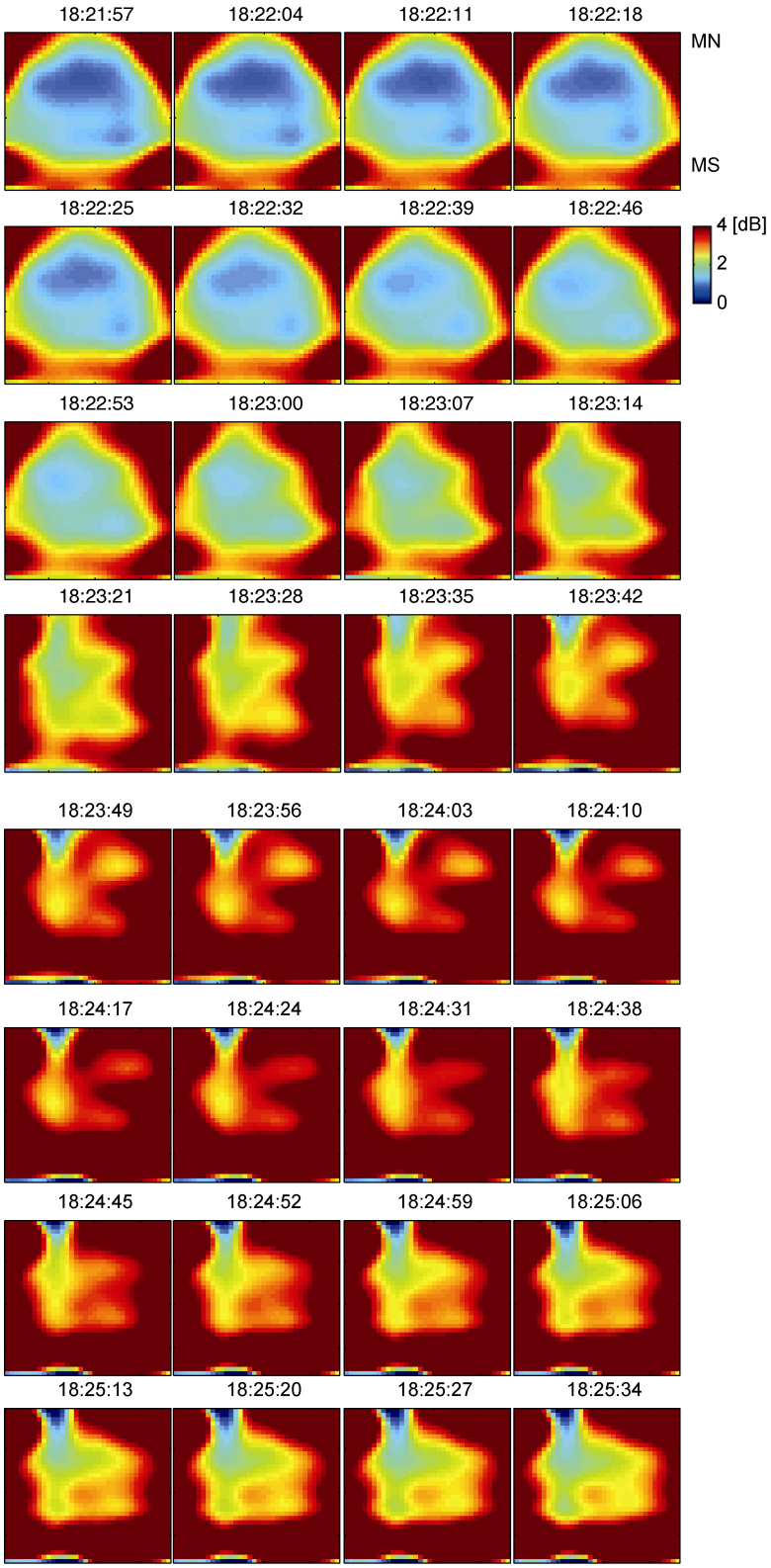

Supplementary Figure 1 2D images of CNA over ZHS with 7 s intervals from 18:21:57 UT to 18:25:34 UT on July 14, 2012.

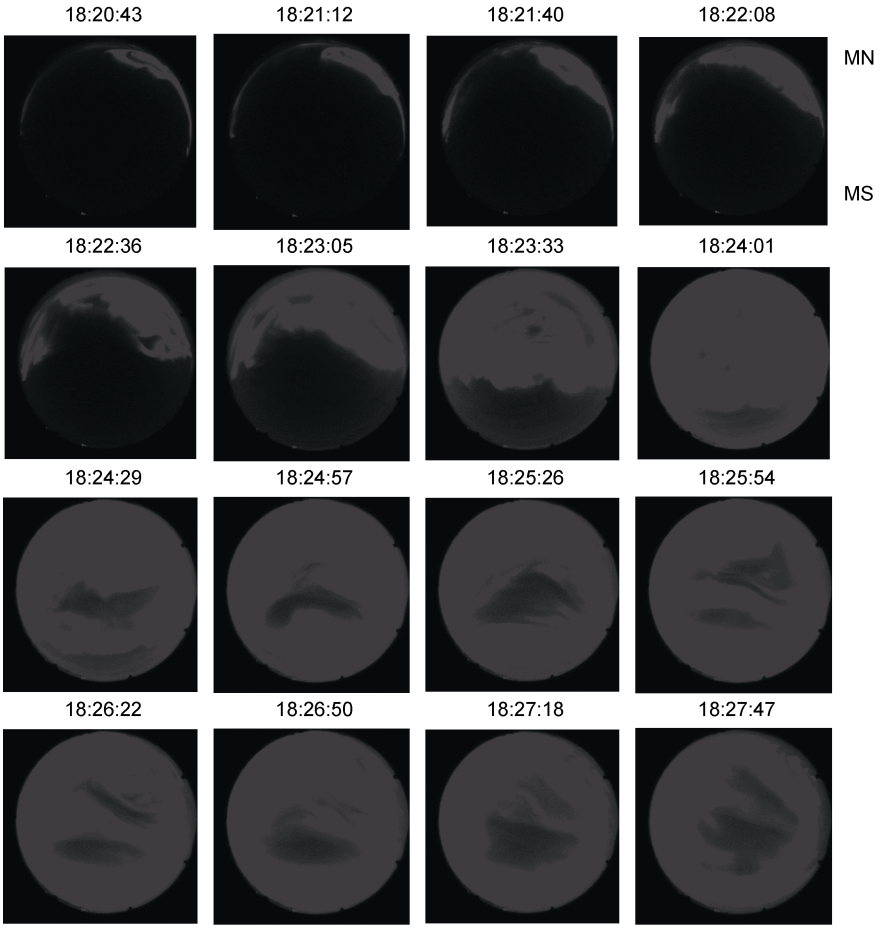

Supplementary Figure 2 Aurora all-sky image over ZHS with λ=557.7 nm with 28 s intervals from 18:20:43 UT to 18:27:47 UT on July 14, 2012.

It can be seen from the all-sky image that the aurora brightened first from the equatorward boundary of the field of view (FOV) at 18:20:43 UT; 170 s later, it expanded rapidly over the middle area of the FOV at 18:23:33 UT. At approximately 18:23 UT, the CNA started to show an evident enhancement area in the FOV. This feature might have led to the CNA commencement occurring three minutes later than that in the ASI observations.